metals

MDPI

Article

Finite Element Modeling and Experimental Verification of a New Aluminum Al-2%Cu-2%Mn Alloy Hot Cladding by Flat Rolling

Alexander Koshmin [1,2,*], Alexander Zinoviev [2], Stanislav Cherkasov [2], Abdullah Mahmoud Alhaj Ali [2,3], Kirill Tsydenov [2] and Alexander Churyumov [4]

[1] Scientific Activity Sector, Moscow Polytechnic University, Bolshaya Semyonovskaya 38, 107023 Moscow, Russia
[2] Department of Metal Forming, National University of Science and Technology MISIS, Leninsky Prospekt 4, 119049 Moscow, Russia; zinoviev@pdss.misis.ru (A.Z.); cherkasov.so@misis.ru (S.C.); makhmud.a@misis.ru (A.M.A.A.); m1900134@edu.misis.ru (K.T.)
[3] Materials Science Department, Moscow Polytechnic University, Avtozavodskaya 16, 115280 Moscow, Russia
[4] Department of Physical Metallurgy of Non-Ferrous Metals, National University of Science and Technology MISIS, Leninsky Prospekt 4, 119049 Moscow, Russia; churyumov@misis.ru
* Correspondence: koshmin.an@misis.ru

Abstract: The roll bonding of an experimental Al-2%Cu-2%Mn alloy with technically pure 1050A aluminum at true deformations of 0.26, 0.33 and 0.40 has been simulated using the QForm 10.3.0 FEM software. The flow stress of the Al-2%Cu-2%Mn alloy has been measured in temperature and strain rate ranges of 350–450 °C and 0.1–20 s^{-1}, respectively. The simulation results suggest that the equivalent strain in the cladding layer is more intense than that in the base layer, reaching 1.0, 1.4 and 2.0 at strains of 0.26, 0.33 and 0.40, respectively. The latter fact favors a decrease in the difference between the flow stresses of the rolled sheet layer contact surfaces by an average of 25% at the highest strain. The experimental roll bonding has achieved good layer adhesion for all the test samples. The average peeling strength of the samples produced at strains of 0.26 and 0.33 proves to be 12.6 and 18.4 N/mm, respectively, and at a strain of 0.40, it has exceeded the flow stress of the 1050A alloy cladding layer. The change in the rolling force for different rolling routes has demonstrated the best fit with the experimental data.

Keywords: finite element modeling; cladding; aluminum alloy; strain–stress state; rheology; peeling strength

Citation: Koshmin, A.; Zinoviev, A.; Cherkasov, S.; Mahmoud Alhaj Ali, A.; Tsydenov, K.; Churyumov, A. Finite Element Modeling and Experimental Verification of a New Aluminum Al-2%Cu-2%Mn Alloy Hot Cladding by Flat Rolling. *Metals* **2024**, *14*, 852. https://doi.org/10.3390/met14080852

Academic Editors: Wenming Jiang and Shusen Wu

Received: 8 July 2024
Revised: 18 July 2024
Accepted: 23 July 2024
Published: 25 July 2024

Copyright: © 2024 by the authors. Licensee MDPI, Basel, Switzerland. This article is an open access article distributed under the terms and conditions of the Creative Commons Attribution (CC BY) license (https://creativecommons.org/licenses/by/4.0/).

1. Introduction

Aluminum-based alloys have gained wide application in a number of industry branches due to their unique combination of performance and relatively low cost [1,2]. Known are a series of heat-treatable Al-Cu system alloys (2219, 2014, 2024 etc.) used as construction materials. These alloys exhibit excellent strength that does not undergo degradation during operation in a wide temperature range [3]. A drawback of these alloys is the necessity of heat treatment, i.e., homogenization before deformation, quenching and long-term artificial aging for the achievement of the maximum possible strength. The fabrication of semi-finished products of these alloys is therefore complicated. There are also indications that their strength decreases significantly during high-temperature operation (at above 200 °C) [4]. The above problems can be solved with a new series of non-heat-treatable Al–Cu–Mn system alloys [5,6] with far higher manufacturability as compared to the Al–Cu system alloys. The authors studied the effect of various alloying additions on the properties of the alloys [7–10], but it was concluded [5] that even without alloying the

base experimental Al-2%Cu-2%Mn alloy exhibits good room-temperature performance and retains it at higher operation temperatures.

Copper-bearing aluminum alloys are highly susceptible to exfoliation corrosion and corrosion cracking [11]. Therefore, the corrosion protection of products made from these alloys includes various types of surface modification, e.g., paint, varnish or polymer application, anodic treatment and cladding with corrosion-resistant aluminum grades. However, the use of anodic treatment or coating for the protection of aluminum construction products has a number of restrictions due to the low strength of the protective layers, which can be damaged even by a weak mechanical impact [12]. Among other variants, the cladding of aluminum alloys with technical-grade aluminum by rolling welding is the simplest method providing reliable protection of the base layer under thermal and mechanical loads.

Despite the relatively long practical experience of hot roll-bonding application for high-strength aluminum alloys and a large number of works on the topic [13,14], the mechanisms of bonding between different metals are not yet completely clear. There are several theories on the formation of strong adhesive bonds between metals as a result of high-pressure treatment, i.e., the "film", diffusion and combined theories [15]. It is, however, doubtless that the key process determining the bonding of metals is joint plastic strain. It is described by the impact duration, stress magnitude, strain magnitude and rate, and process thermal conditions [16].

Calculation methods have been used for studying the formation of bonds between different and similar metals by rolling techniques since the middle of the last century. However, FE-based analysis has undergone rapid development only in last few decades. The advancement of FE methods in this field would facilitate the precise determination of metal bonding, thereby enabling the accurate prediction of the resulting product quality. Good results of cold-cladding simulation were achieved using the Zhang–Bay model [17,18] and the cohesive zone model (CZM) [19,20]. These models allow prediction of the metal layer bond strength with a good accuracy and are widely used for the solution of the planar (2D) task. Moreover, 3D simulation is used much less frequently due to its high time consumption, but there are some 3D simulation works, including those conducted using the QForm software [21,22]. Their results indicate the applicability of the QForm software for joint strain simulation for at least two objects.

However, there are no published works dealing with the roll bonding of metal layers from the viewpoint of the influence of the deformation center (DC) shape and size, temperature, force and strain rate on the bonding of flat-rolled layered sheets. The aim of this work is to study the plastic parameters of the Al-2%Cu-2%Mn alloy, develop and implement a finite element model of its cladding with technically pure aluminum at different strain parameters, and analyze the results by comparing them with experimental roll-bonding data.

2. Materials and Methods

2.1. FE-Modeling Methods

Hot roll bonding (cladding) was simulated in 3D problem mode in accordance with the principles of plastic deformation, with the elastic properties excluded from the analysis. The geometrical parameters of the tool, along with the parameters of a DUO 21 × 300 rolling mill (Figure 1a), were imported into the QForm software using the tetrahedral shape of FEs. The workpieces were two individual sheets of 50 mm in width and length, with three combinations of base and cladding layer thicknesses: 5.85 and 0.65, 6.3 and 0.7, 6.75 and 0.75 mm. The roll gap was 5 mm in each case. The contact stress and flow rate were studied using tracked points in the middle of the workpiece width, and, over the workpiece thickness, at the contact between the base (P1) and cladding (P2) layers, at the contact between the base layer and the lower roll (P3) and in the middle of the overall rolled workpiece thickness (P4), see Figure 1b. Figure 1c schematically illustrates the DC

and the length of the arc-shaped metal/roll contact point trajectory relative to the X-axis (X/L_{dc}). The simulation data were analyzed and the curves were plotted for that section.

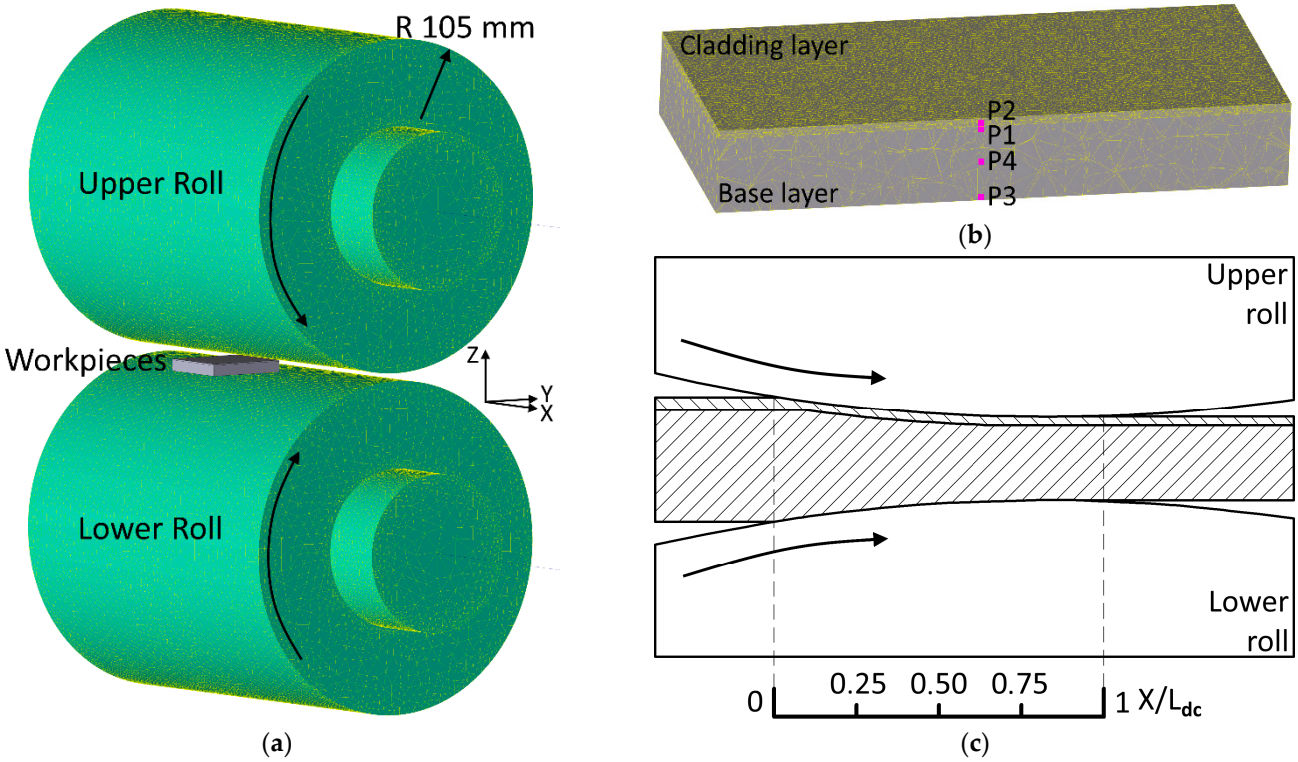

Figure 1. Roll unit (**a**), view of the central longitudinal workpiece section (**b**) and schematic of the deformation center (**c**).

The calculation accuracy was improved by adaptable reconstruction of the calculation mesh, with the mesh adaptation coefficient for the workpieces being accepted at 1.5. Thus, the ratio between the maximum size of the simulated object and the size of any finite element mesh element was within the preset range. The key input parameters of the model are summarized in Table 1.

Table 1. Input parameters of the workpiece and tool models.

Model Parameters	Value
Roll material	41Cr4
Roll temperature, °C	25
Workpiece temperature, °C	400
Ambient temperature, °C	25
Number of tool finite elements, ths. pcs.	135
Number of workpiece finite elements at start/end of simulation, ths. pcs.	167/377
Time step, ms	0.7

The contact interaction of the workpiece/workpiece and workpiece/tool pairs was described using Siebel's law representing the tangential stresses (τ) at the workpiece surface as the product of the friction factor (k_f) and the flow stresses of the workpiece layers contacting with the tool and with the other workpiece (σ):

$$\tau = k_f \frac{\sigma}{\sqrt{3}}. \quad (1)$$

The friction factor was studied experimentally by measuring the rolling time for samples of alloys similar to the test ones and comparing that time with the model time.

Furthermore, the changes in the shapes of the sheet butt-ends and side edges were compared. The friction factor was set to be 0.75 for the workpiece/tool pair and 0.98 for the workpiece/workpiece pair. The workpiece/workpiece pair friction factor was set large, taking into account the special pre-treatment of their contact surfaces, i.e., degreasing and mechanical treatment (for greater roughness).

QForm uses a special contact element for the numerical simulation of the joint deformation of two objects (workpieces) because the finite element mesh nodes of contacting bodies generally do not match. Figure 2 schematically shows the principle of that interaction. The normal direction is shown by the vector $\vec{n}$. The node variables are the node velocities (v_p). Then, the normal force function P_n that minimizes the penetration along the normal to the workpiece contact surfaces is as follows:

$$P_n = C\left(v_n^{k1} - v_n^{p}\right), \tag{2}$$

where C is the penalty coefficient, i.e., a parameter exceeding the greatest of the rigidity matrix diagonal coefficients for both the contacting bodies. Thus, one can find the forces in the nodes of the contacting element using the form functions as follows:

$$P_n = P_n^{k_1} - P_n^{i_2} - P_n^{j_2} - P_n^{k_2}. \tag{3}$$

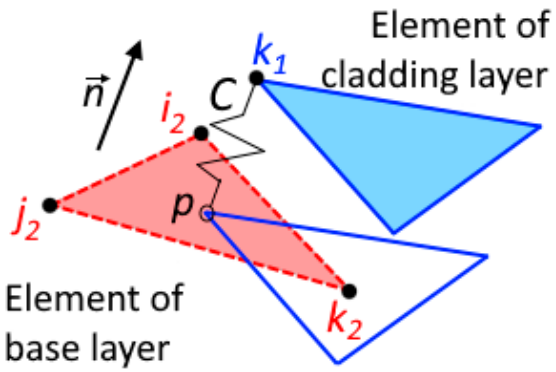

Figure 2. Schematic of the contacting finite elements for two workpieces [23].

2.2. Materials Characterization

The materials studied were technically pure 1050A-grade aluminum (EN 573-3:2007 [24]) for the cladding layer and the experimental Al-2%Cu-2%Mn alloy (hereinafter, 2Cu2Mn) for the base layer. The charge for casting ingots of the required composition was technically pure aluminum (99.97%), oxygen-free copper (99.9%) and Al-10%Mn master alloy. The charge was melted in a muffle furnace at 750 °C, in a fire-clay crucible. The melt was cast into 20 × 130 × 180 mm graphite molds for the 2Cu2Mn alloy and 10 × 75 × 180 mm ones for 1050A. The ingots were sampled for the chemical composition spectral analysis. The as-cast structure of the experimental alloy (Figure 3) contains the Al_2Cu and Al_6Mn eutectic phases in the form of globular particles and veils, respectively. The chemical compositions of the alloys are summarized in Table 2.

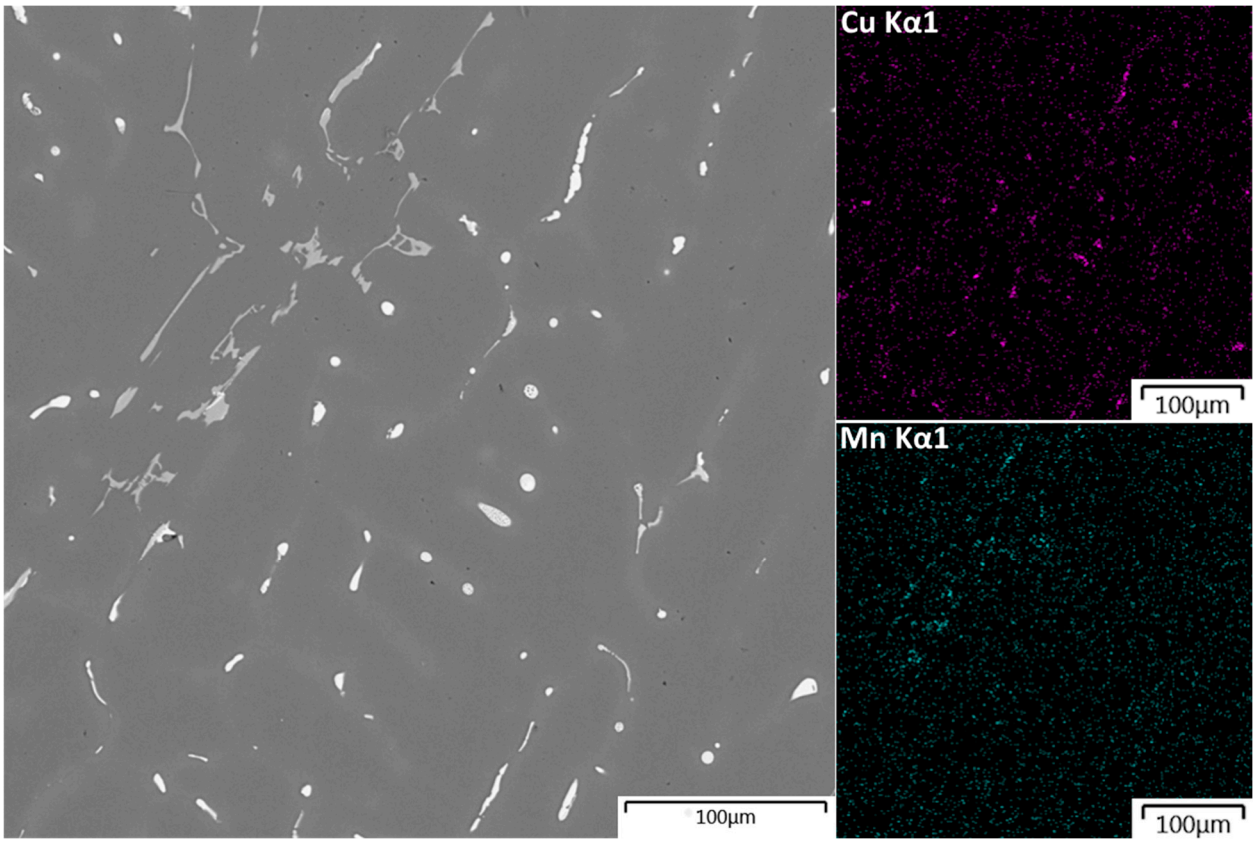

Figure 3. Microstructure and EDS maps of the 2Cu2Mn alloy.

Table 2. Chemical composition of the test alloys (wt.%).

Alloy	Al	Cu	Mn	Si	Fe
2Cu2Mn	Base	1.93 ± 0.05	1.94 ± 0.04	0.05 ± 0.04	≤0.01
1050A	Base	-	-	0.18 ± 0.03	0.03 ± 0.02

2.3. Experimental Procedure

The 2Cu2Mn alloy ingot was first rolled at 400 °C in a DUO 210 × 300 two-roll mill to a 10 mm thickness for structure deformation. Then, 5 × 10 mm cylindrical samples were cut from the as-rolled sheet in the transverse vertical direction for studying the rheological parameters with the quenching/deformation unit of a DIL805A/D dilatometer. The test temperatures and strain rates were chosen based on the hot deformation conditions typically used for treating the test alloy, i.e., the temperatures T = 350, 400 and 450 °C and the strain rates $\dot{\epsilon}$ = 0.1, 1, 10 and 20 s^{-1}. Given the high precision with which the intermediate values in the experiment matrix can be calculated, it was deemed unnecessary to perform the experiment for the two cases, T 400 °C, $\dot{\epsilon}$ 1 s^{-1} and T 400 °C, $\dot{\epsilon}$ = 10 s^{-1}. The samples were compression tested to a true strain (ε_t) of 0.9. The resultant test alloy strengthening curves (Figure 4) were corrected for friction and temperature, and the coefficients of the deformation resistance (σ) equation were calculated with an allowance for thermal softening [25]:

$$\sigma = \exp(A) \cdot \dot{\epsilon}^m \cdot \varepsilon_t^{n_1} \cdot \exp(\varepsilon_t \cdot n_2) \cdot \exp(T \cdot l), \quad (4)$$

where A, m, n_1, n_2 and l are the coefficients describing the material properties.

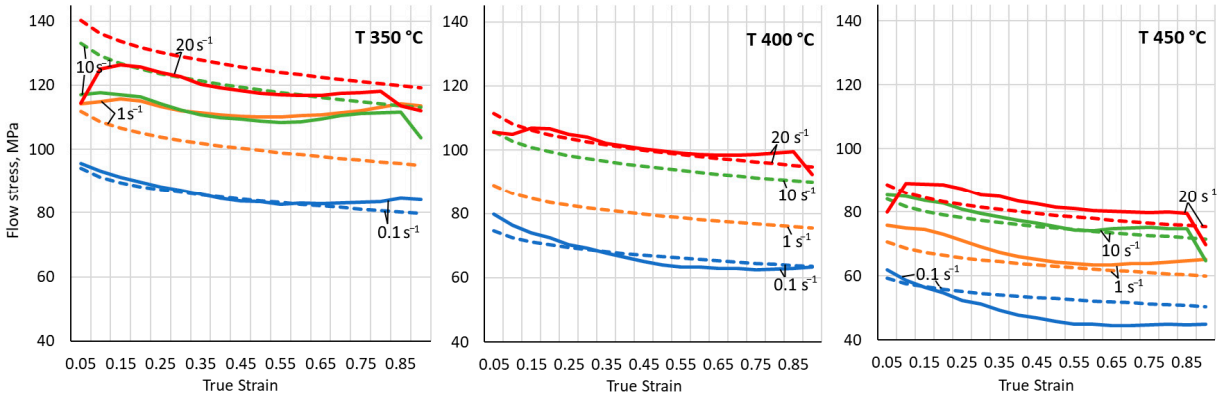

Figure 4. Experimental (solid) and calculated (dashed) flow stress curves of the 2Cu2Mn alloy.

The calculated coefficients for the alloys are summarized in Table 3, along with the calculated relationship coefficients R^2.

Table 3. Hot-rolling deformation resistance coefficients.

Alloy	A	m	n_1	n_2	l	R^2
2Cu2Mn	6.2121	0.0756	−0.0382	−0.0046	−0.0616	0.9678
1050A	4.9577	0.1475	0.1607	−0.0035	−0.0174	0.9744

An indispensable experimental alloy parameter for simulation is the heat conductivity. It was calculated using the Wiedemann–Franz law:

$$\frac{k}{\gamma} = L \cdot T, \quad (5)$$

where k is the heat conductivity (W/m·K); γ is the electrical conductivity (S/m); and L is the Lorentz number, which is $2.23 \cdot 10^{-8}$ W·Ohm·K^{-2} for aluminum alloys [25].

The room temperature electrical conductivity of the 2Cu2Mn alloy was measured with an eddy current structurescope. The result was $15.3 \cdot 10^6$ S/m. The electrical conductivity γ of the model alloy for elevated temperatures was obtained by extrapolating the available data [26] relative to the experimental result. Thus, the calculated heat conductivity of the model alloy was 161, 159 and 151 W/(m·K) for 350, 400 and 450 °C, respectively. The heat conductivity of the 1050A alloy cladding layer was sourced from the standard QForm deformable materials library and was 226 W/(m·K). It was assumed that the specific heat of the 2Cu2Mn and 1050A alloys were 838 and 930 J/(kg·K), respectively.

The base and cladding layer ingots of the 2Cu2Mn and 1050A alloys, respectively, were rolled in the DUO 210/300 mill to three different initial workpiece thicknesses, as described in the Section 2.1. Thus, subsequent rolling of the assembled workpieces for all the test thickness variants to a final thickness of 5 mm provided for true strains (ε_t) of 0.26, 0.33 and 0.40 (Table 4). The workpiece thicknesses were chosen so as to have a final cladding layer thickness of 10% of the overall final workpiece thickness. The sheet surfaces were pre-treated for cladding, i.e., mechanically treated with metal brushes and degreased with perchloroethylene (C_2Cl_4), and the corners of each assembled workpiece were fastened with wires to avoid layer shift upon roll clamping. The final assembled workpieces were rolled at 400 °C.

Table 4. Dimensions of the cladding workpieces.

Route	Base Layer Thickness	Cladding Layer Thickness	Total Thickness	ε_t
I	5.85 mm	0.65 mm	6.5 mm	0.26
II	6.30 mm	0.70 mm	7.0 mm	0.33
III	6.75 mm	0.75 mm	7.5 mm	0.40

The final sheets were sampled for the metallographic analysis and mechanical tests. The microstructure of the alloys was examined under a TESCAN VEGA 3 SEM, the phase composition was studied with an OXFORD Aztec EMPA and the microhardness was tested with a MH-6 Vickers hardness tester (Metkon Instruments Ltd., Bursa, Turkey) at a 25 g load and a 10 s dwell time. The ultimate tensile strength, yield stress and elongation tests were conducted on an Instron 5900 Series universal tester at a tension rate of 0.001 s^{-1}. The tension test material was sampled along the rolling direction. The layer bonding strength was assessed with a method similar to the peeling test (T-Peel test, ASTM D1876 [27]). The peeling test microsamples were 5 mm in width and 30 mm in length, taken from the mid-width section of the sheets. The tests were stopped when a steady state was achieved.

3. Results

3.1. Simulation Results

3.1.1. Temperature

The thermal fields in the workpieces formed similarly, regardless of the deformation (Figure 5). Upon entering the DC, the metal temperature dropped almost immediately by an average of 50 °C at the contact with the tool. As the workpieces moved farther along the rolling axis, the temperatures in their contact zones equalized steadily, tending to the temperature of the inner non-contacting zone. This was favored by deformation heating of the base layer, which did not reduce but on the contrary increased its temperature by an average of 10 °C above the initial temperature. Cladding layer cooling attracts special attention (Figure 5b, P2 (refer to Figure 1b)). Upon contact with the tool, the cladding layer temperature decreased over the entire layer thickness, but the temperature decrease did not extend into the base layer (Figure 5b, P1 (refer to Figure 1b)), whose temperature remained high. This fact can be accounted for by specific features of the software heat transfer calculation procedure, which is individual for each workpiece and does not allow for excluding the pause coefficient after passing the deformation center. In other words, the model used does not account for the formation of a weld joint (adhesion) between the layers. Nevertheless, the data on the temperature change in the rolled layers seem to be plausible. The temperatures of the layers near the contact zone always tend to equalize as soon as after 20–30 ms after sheet release from the DC.

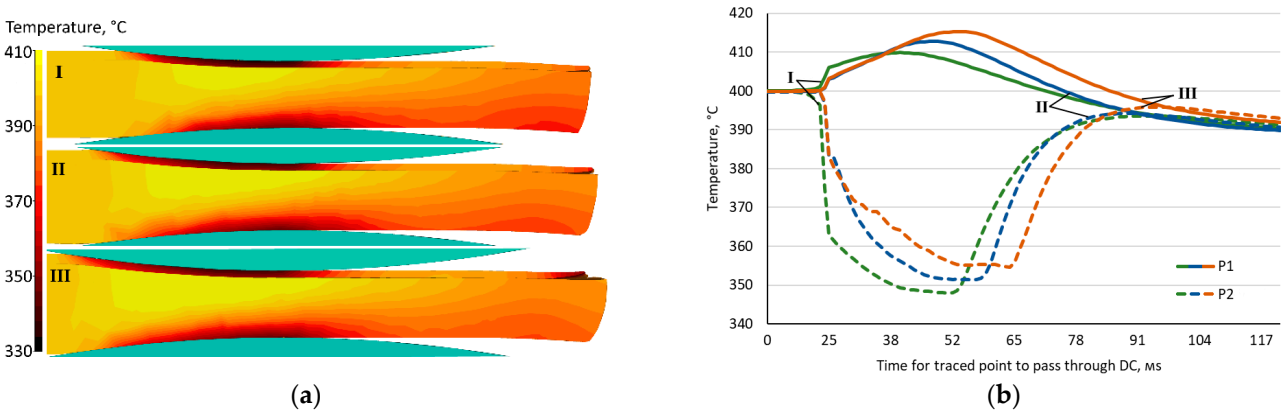

Figure 5. Thermal fields in the deformation center (**a**) and temperature of the base (P1) and cladding (P2) layers during rolling (**b**).

3.1.2. Rolling Force and Torque

The rolling force curves (Figure 6a) clearly show all the process stages, i.e., workpiece clamping by the rolls, steady-state stage and metal release from the rolls. The steady-state forces are 75, 90 and 105 kN for Routes I, II and III, respectively. There is a clear trend of increasing the rolling force by 20% with each 0.5 mm deformation increment. The rolling

torque changes less predictably. Its curve also exhibits peaks corresponding to metal clamping and release from the rolls, but the steady-state stage features multiple oscillations originating from the presence of two objects in the DC, the contact friction between which varies along the DC. Another specific feature is the difference in the rolling torques for the upper and lower rolls. The lower roll torque at the contact with the base layer is on average two times higher than the upper roll torque at the steady-state rolling stage for all the test samples. This is obviously caused by the difference in the flow stresses of the test alloys, which directly affects the contact friction conditions. However, comparison between the rolling forces at the lower and upper rolls for all the simulation cases reveals a smaller difference, within 10%.

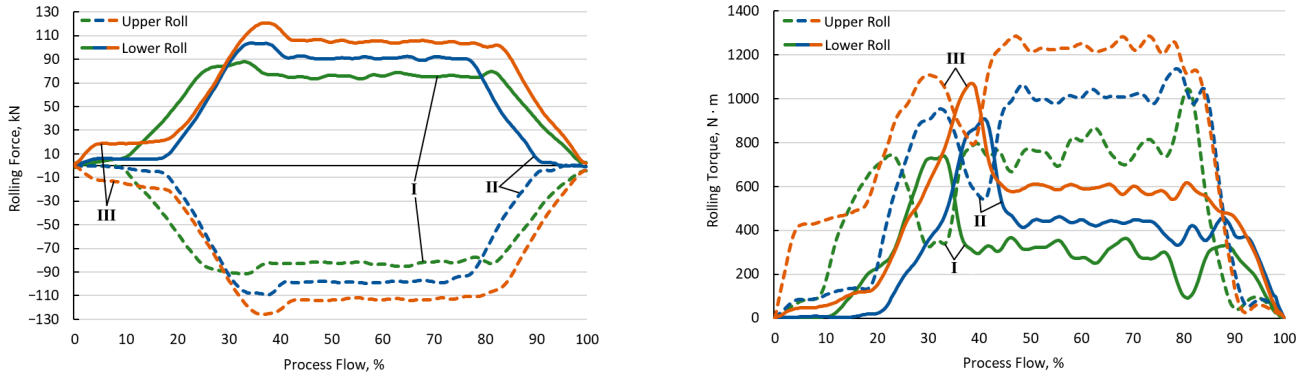

(**a**) (**b**)

Figure 6. Changes in the rolling force (**a**) and torque (**b**).

3.1.3. Stress–Strain State

The patterns of the equivalent strain formation (ε_{eq}) and equivalent strain rate distribution ($\bar{\varepsilon}_{eq}$) along the DC are shown in Figure 7. It can be seen that the strain magnitude greatly affects the above parameters. An increase in the strain noticeably increases the DC length and hence the contact duration of the bonded surfaces under pressure. The base layer strengthening with an increase in ε_t is less intense as the cladding layer strengthening, due to a more intense cladding layer cooling and a different equivalent strain rate distribution. The equivalent strains in the cladding layer contact zone were 1.0, 1.5 and 1.9 for Routes I, II and III, respectively. The equivalent strain rates were roughly the same in all cases, i.e., within 80 s^{-1} at the DC entrance in the maximum deformation zone and within 15 s^{-1} in the middle of the DC height (and on average along the entire DC). The $\bar{\varepsilon}_{eq}$ distribution fields also allow for making some observations. The deformation is the most intense at the DC entrance and exit. The lengths of these zones differ between the samples, but their percentage relative to the entire DC length remains the same. One can also distinguish impeded deformation zones at about 0.7 of the DC length. The illustrative $\bar{\varepsilon}_{eq}$ distributions (X-shaped) originate from the metal flow pattern and the accompanying development of shear strains in these zones.

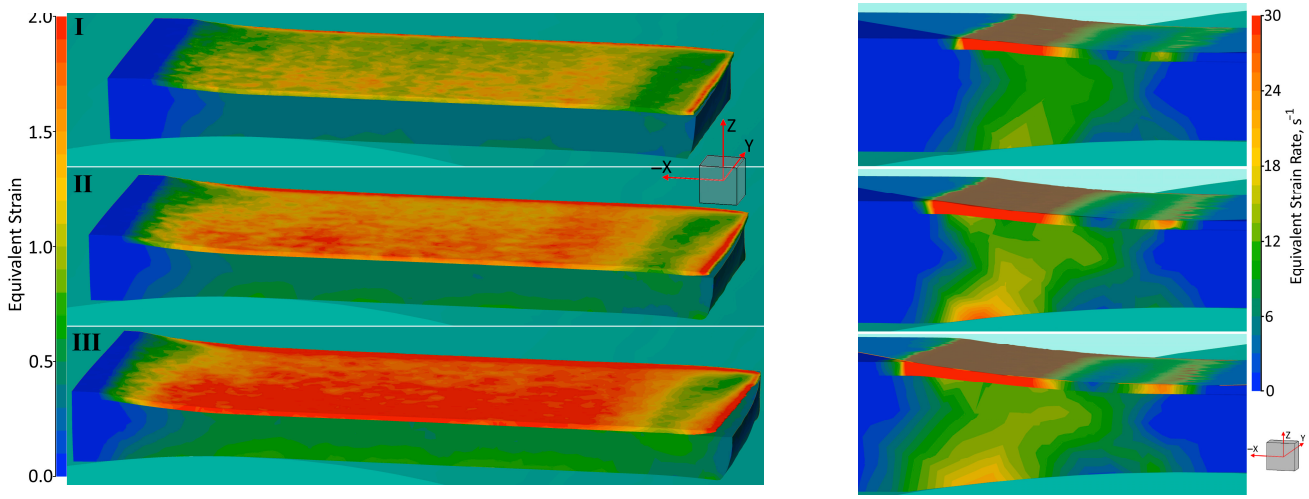

(**a**) (**b**)

Figure 7. Equivalent strain (**a**) and equivalent strain rate (**b**) fields in DC for different routes.

Many researchers [28,29] reported regularity in the adhesion of layered rolled sheet surfaces differing in hardness or strength. Their results suggest that a large difference in the strengths of the contact surfaces between bonded sheets favors nonuniform metal flow at the workpiece surfaces relative to each other within the deformation center. This generates additional tangential stresses between the layers, thus reducing the effect of normal stresses, resulting in a failure to produce a strong weld joint. Furthermore, relying upon the "film" metal bonding theory, one can hypothesize that the high strengths of the contacting surfaces favor more efficient fracture of the oxide films upon deformation and the bonding of the juvenile (oxide-free) areas forming as a result. Figure 8 shows the change in the flow stress (σ) of the base and cladding layers along the DC. It should be noted that the DC length relative to the rolling axis is the same for all the test samples, but its actual length and hence the duration of contact under rolling force increases by approx. 15% with each 0.07 true deformation increment. It can be seen from the curves that the deformation resistances of both layers change, albeit slightly, with deformation. They are on average 90 and 60 MPa for the base and cladding layers, respectively. However, the most important factor that can be traced from the curves (Figure 8, I–III) is the permanent softening of the base layer and the strengthening of the cladding one. This change in the metal properties along the DC is in a good agreement with the above-described rolling temperature conditions (Figure 5) and the role of the equivalent strain (Figure 7a). For all the test samples, σ decreases by approx. 20% at 0.55–0.75 of the DC length and then restores to the previous level, which is retained until metal release from the rolls. This can be accounted for by the fact that the tracked points pass the relatively low equivalent plastic strain rate zones (blue zones in Figure 7b) and by the overall decrease in the normal and tangential stresses in that zone. Comparing the difference in the deformation resistances for the surfaces of each layer (~~$\Delta\sigma$, Figure 8d~~ Figure 8, $\Delta\sigma$), one can see their steady decrease with an increasing strain. Obviously, the lowest $\Delta\sigma$ is achieved at a 0.40 strain. The curves suggest that the strengths of the layer surfaces are equalized due to the cladding layer strengthening and base layer softening caused by heating. The strengthening of the cladding layer results in a pronounced reduction in $\Delta\sigma$, commencing from the 0.70 X/L_{DC} point and reaching a minimum at length 0.85. This is due to the complex strain–temperature effect, particularly a sharp increase in the strain rate beyond the region of its decrease, marked in Figure 7b, and the continued cooling of the cladding layer in contact with the roll. After reaching the indicated point 0.85, the strain rate decreases markedly and the temperature due to heat transfer equalizes, which contributes to the return of the curve to the previous values.

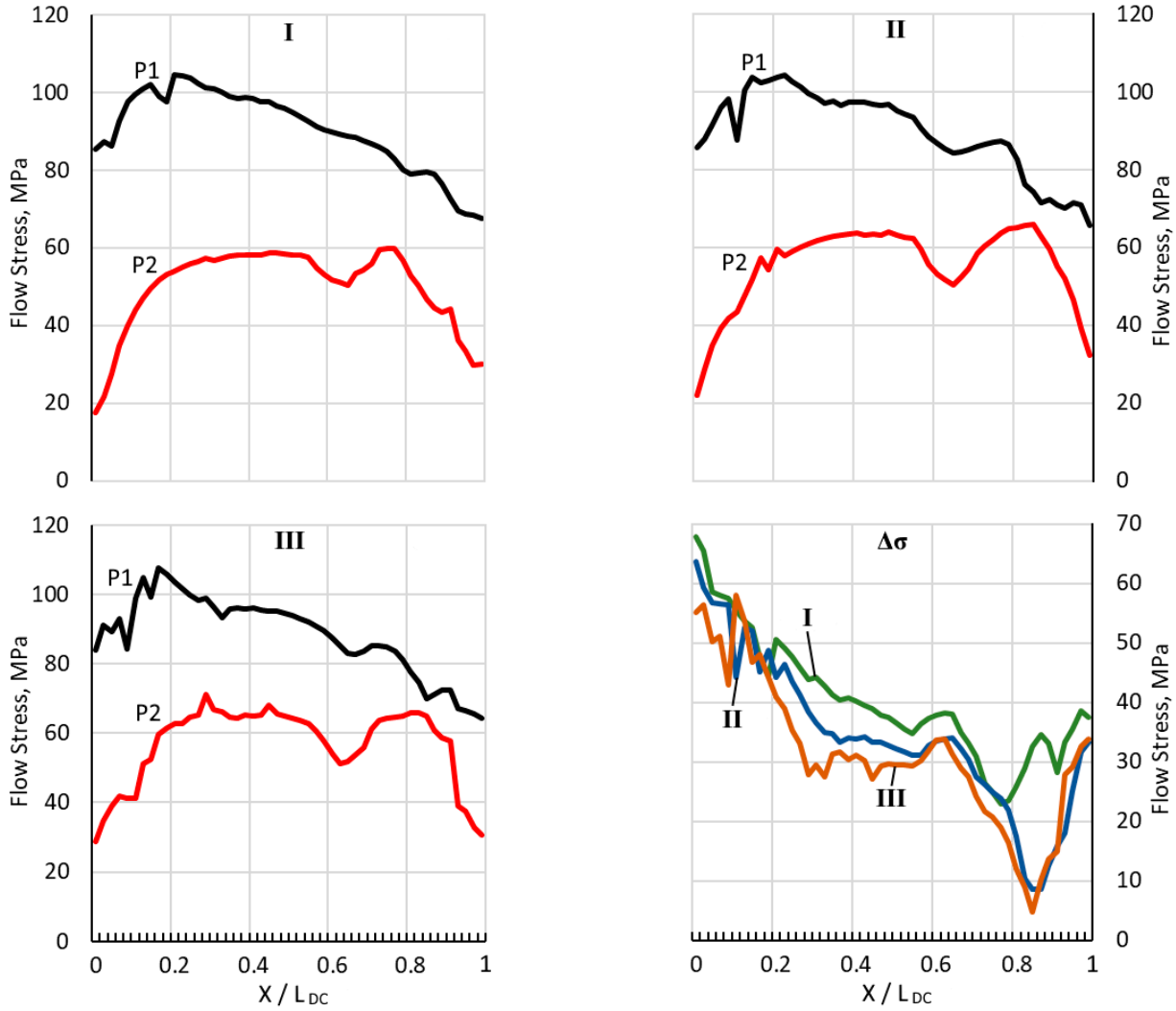

Figure 8. Change in deformation resistance of the base (P1) and cladding (P2) layers and the difference in their deformation resistances (Δσ) along the deformation center.

3.1.4. Surface Interaction

The multiple rolling process parameters that act during the joint deformation of two workpieces and are nonuniform in the DC length and height, e.g., temperature, flow rate, strain rate, layer surface strength, etc., increase the tangential stresses at the interlayer boundary. Their effect on the formation of composite bonds was assessed using the standard QForm subroutines, "Pressure" and "Friction", for calculating the normal pressure stress (σ_P) and the tangential friction stress (τ_f). The calculation results are shown in Figures 9 and 10. The calculations covered not only the DC but also the foregoing section in which there is yet no strain but flat rolling stresses already start to develop. The pressure curve shows that it grows in all the test samples in the –0.17–0.30 X/L_{DC} section, where the decrease in the rolled sheet thickness is the greatest. This section is followed by a slight decrease in the pressure and its further steady growth to the maximum point at 0.7 DC length. The highest normal pressure (275 MPa) is achieved for rolling via Route III. The normal pressure grows on average by 10% with a 0.07 true strain increment. The normal pressure distribution in the DC lateral direction (Figure 9b) does not exhibit peaks, in contrast to the central section. The pressure decreases steadily in the DC zone toward the sheet edges, reaching a minimum value of 100 MPa in the near-edge zones. The normal pressure in the zones at 8 and 16 mm distances from the central section decreases steadily, on average by 10 and 40%, respectively.

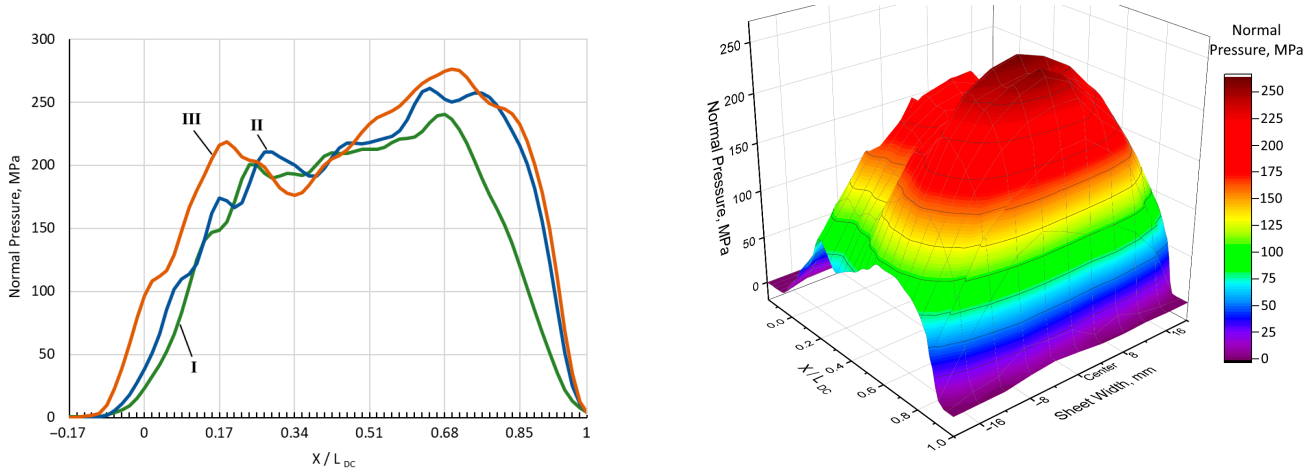

(**a**) (**b**)

Figure 9. Change in normal pressure between the rolled sheet layers along the deformation center (**a**) and over the entire DC area for ε_t= 0.33 (**b**).

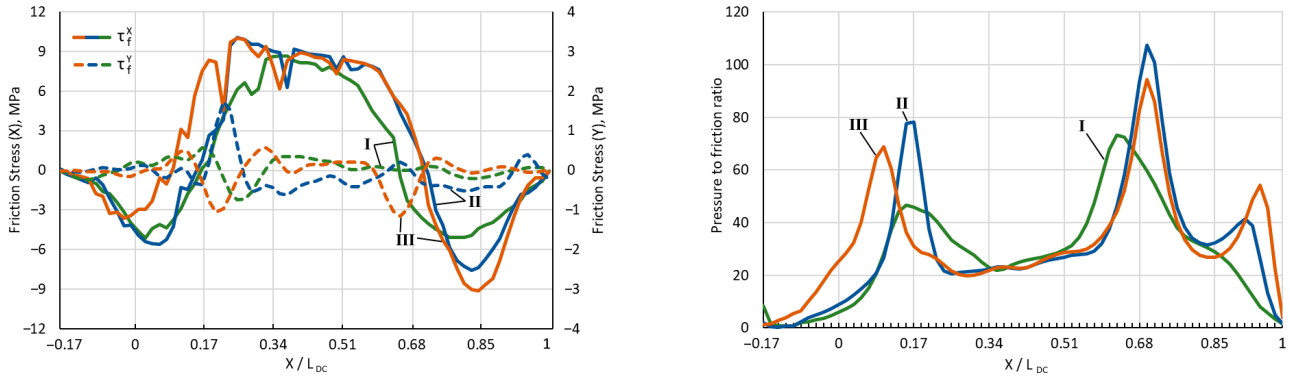

(**a**) (**b**)

Figure 10. Change in friction stress along (τ_f^X) and across (τ_f^Y) the rolling axis (**a**) and ratio of pressure forces to friction forces between the layers along the DC (**b**).

The change in the friction stress has a different pattern (Figure 10a). Obviously, the friction stress at each DC point of the test samples can differ from the simulated one due to the multiple weakly controlled contact interaction factors in the case of two jointly strained workpieces. However, it is clear that the overall pattern of the stress distributions along the DC remains the same for rolling at different ε_t. As to the friction stress pattern along the rolling axis (τ_f^X), one can distinguish four typical sections: the DC entrance zone (–0.17–0.00 X/L_{DC}), the backward slip zone (0–0.25 X/L_{DC}), the no-slip zone where the strain is the highest (0.25–0.75 X/L_{DC}) and the forward slip zone (0.75–1.00 X/L_{DC}). The friction stress grows in the first zone in the direction opposite to the rolling one. Upon DC entrance, the friction stress between the workpieces reorients to coincide with the rolling direction and grows steadily to 8–10 MPa until the workpieces enter the no-slip zone. The stress in the latter zone is constant. At the no-slip zone boundary, the friction stresses at the workpiece surfaces reach 0 MPa and then become negative again, eventually growing back to zero upon the release from the DC zone. The friction curve along the Y-axis (widening direction) has peaks at the no-slip zone boundaries. The friction stress along the Y-axis varies on average within −1 to 1 MPa.

Figure 10b shows the σ_P vs. τ_f^X curve. For all the test samples, the curve has two typical peaks at 0.17 and 0.7 DC length. Both peaks correlate with the extrema in the curve shown in Figure 9a. The former peak is caused by the start of weld joint formation between the layers, accompanied by an increase in the plastic strain of the base layer at that point.

The latter one originates from the improvement of the contact interaction conditions at that section, i.e., a lower strain rate and the respective decrease of τ_T to zero. It is safe to assume that the layer-bonding work is the greatest at that point under normal stresses. The stress ratio in the no-slip zone is generally constant and approximately the same for the test samples.

3.2. Experimental Results

3.2.1. Microstructure

Figure 11 shows microstructural and layer boundary images. The layer boundaries of the test samples have no discontinuities, suggesting good metal bonding. The base layer structure is saturated with Al_2Cu-phase particles, the average sizes of which increased to 1–2 μm as a result of deformation. Some boundary regions contain larger 4–8 μm particles, some of which are located directly at the layer boundary (Figure 11c) and contact with the cladding layer metal. However, the EDS data for these regions showed no migration of the base layer alloying additions (Cu and Mn) to the cladding layer, suggesting that the adhesion of the layers occurs by a deformation mechanism rather than a diffusion one. Furthermore, the images of the deformed sheets do not show any clear traces of the Mn-containing phase. The veils occurring in the ingot structure (Figure 3) were greatly refined as a result of the deformation and temperature.

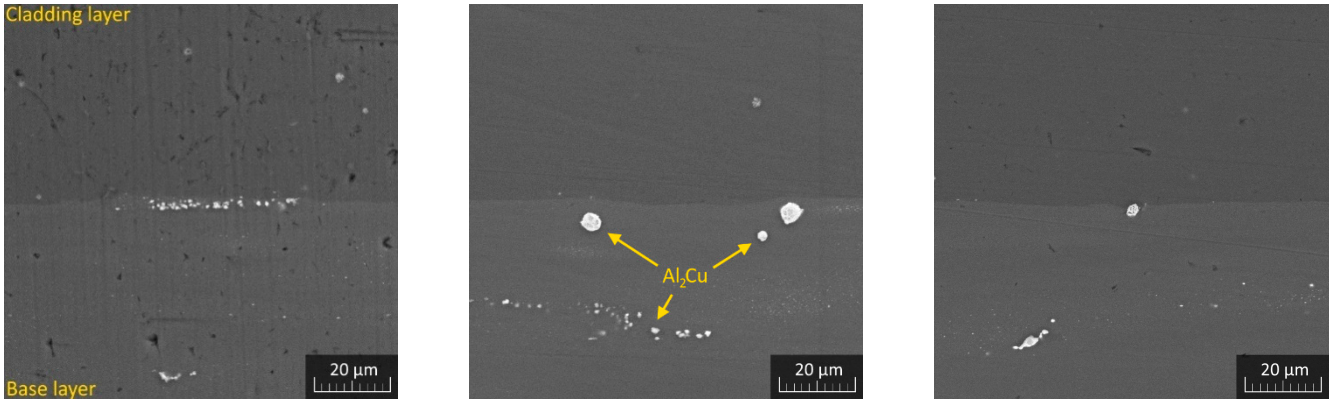

(**a**) (**b**) (**c**)

Figure 11. SEM microstructural images of the layer boundary in roll bonded sheets after deformation via Routes I (**a**), II (**b**) and III (**c**).

3.2.2. Mechanical Properties

The microhardness of the roll-bonded samples was measured over sample thickness at variable steps (Figure 12a). The average microhardness was 61 HV for the base layer and 29 HV for the cladding one. No change in the microhardness was observed at the layer boundary. It can be seen from the curve that the microhardness of the layers depends on roll-bonding strain, albeit slightly. Furthermore, it was almost constant over the thickness of the layers except for some regions in the middle of the layered rolled sheets. There, the microhardness dropped to 55 HV, probably due to deformation heating localization at those points.

The tensile tests of the roll-bonded sheets did not show any effect of the strain magnitude on the mechanical properties (Figure 12b). The average yield stress, ultimate tensile strength and elongation were 160 MPa, 230 MPa and 16%, respectively. Comparing the experimental data with earlier data for Al–Cu–Mn system alloys, one can conclude that the strength of the roll-bonded sheets is 50 MPa lower as compared to those in a hot-deformed state [5]. The plasticity of the material is on average 5% higher.

It is well known that the ultimate tensile strength of roll-bonded sheets can be calculated using the following formula [30]:

$$\Delta UTS = \frac{H}{100}(UTS^{BL} - UTS^{CL}), \quad (6)$$

where H is the thickness of the cladding layers, % of the overall sheet thickness, UTS^{BL} is the ultimate tensile strength of the base layer, MPa, and UTS^{CL} is the ultimate tensile strength of the cladding layer, MPa.

Thus, the latter formula is not applicable to the cladding of the test alloy since the calculation result is 2.5 times lower than the actual one.

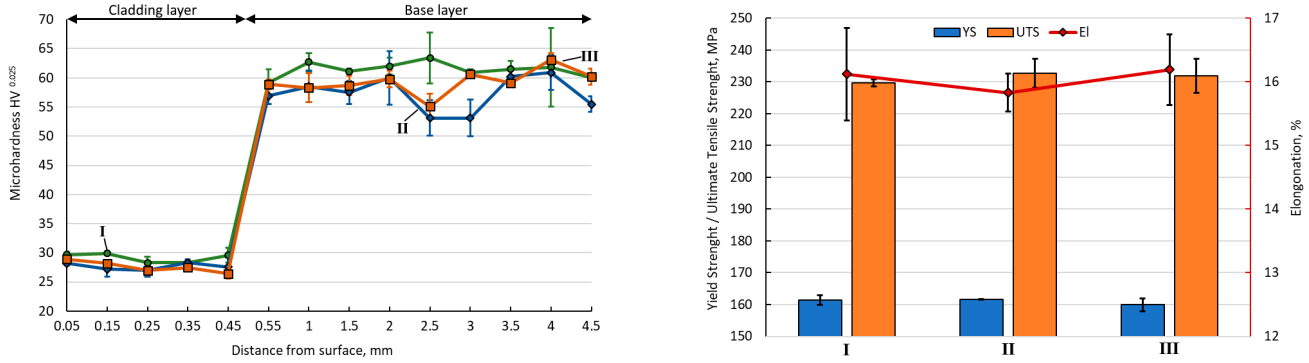

(**a**) (**b**)

Figure 12. Microhardness over thickness (**a**) and yield stress (YS), ultimate tensile strength (UTS) and elongation (El) (**b**) of the test samples.

3.2.3. Bonding Characteristic

The interlayer boundary in the sample region destructed as a result of the tensile tests was studied under SEM (Figure 13). SEM allows for characterizing the quality of the bonding between the metal layers by features revealed upon joint tension of materials with different mechanical properties. The sheet bonded at a 0.26 true strain contained mainly large cavities between which thin coupling bridges occurred (Figure 13a). The bridges are typical of an early stage of bonding. With a 0.07 increase in the strain, the number and regularity of the bridges between the layers increased noticeably to form interlayer bonding. However, there were still some cavities sized 1000–2000 μm². At a 0.4 strain, the sheet surface-tearing areas (Figure 13c) had quite smooth interlayer boundaries, indicating uniform elongation of the materials in these areas and hence good interlayer bonding. Bonding discontinuities still occurred, but their total area was 1.5–2 times smaller than for deformation Route II.

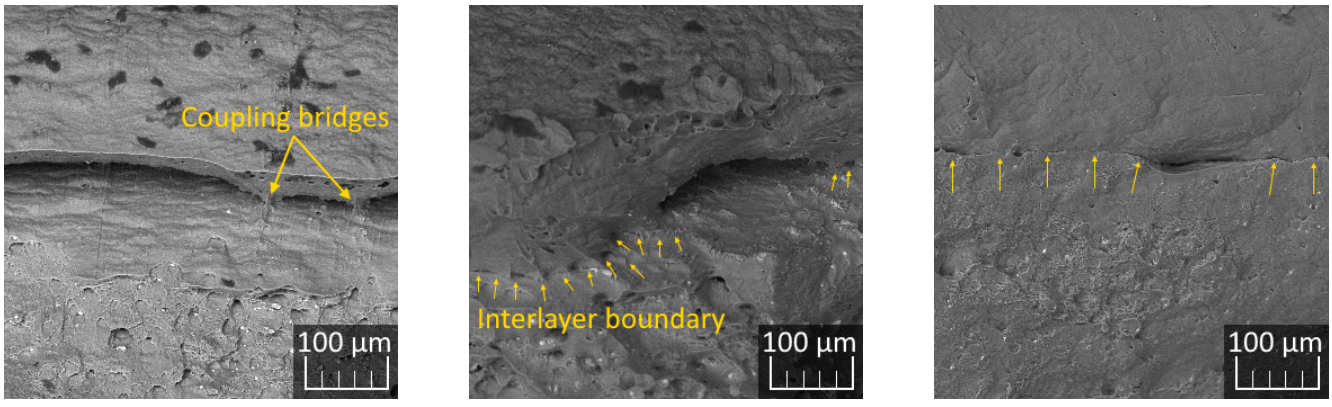

(**a**) (**b**) (**c**)

Figure 13. SEM images of the interlayer boundaries after the tensile tests for samples roll bonded via Routes I (**a**), II (**b**) and III (**c**).

Figure 14 shows the peeling test data. The average layer-bonding strengths for cladding at true strains of 0.26 and 0.33 were 12.6 and 18.4 N/mm, respectively. Testing of the sample roll bonded at a strain of 0.4 did not cause cladding layer peeling. Instead, a tension curve of the technically pure aluminum cladding layer was observed, and the cladding layer underwent fracture at a 39 N/mm load, in agreement with the UTS of the 1050A alloy, which is 80 MPa. The latter result indicates the formation of interlayer bonding, the strength of which is higher than that of the cladding layer. At the steady-state peeling stage (0.33 strain), one can clearly see curve oscillations within 0.4–0.6 N/mm caused by the regular occurrence of cavities in the peeling zone. The absence of oscillations for a 0.26 strain can be accounted for by the generally lower bond quality, i.e., a large number of cavities and a small overall area of coupling bridges between the layers.

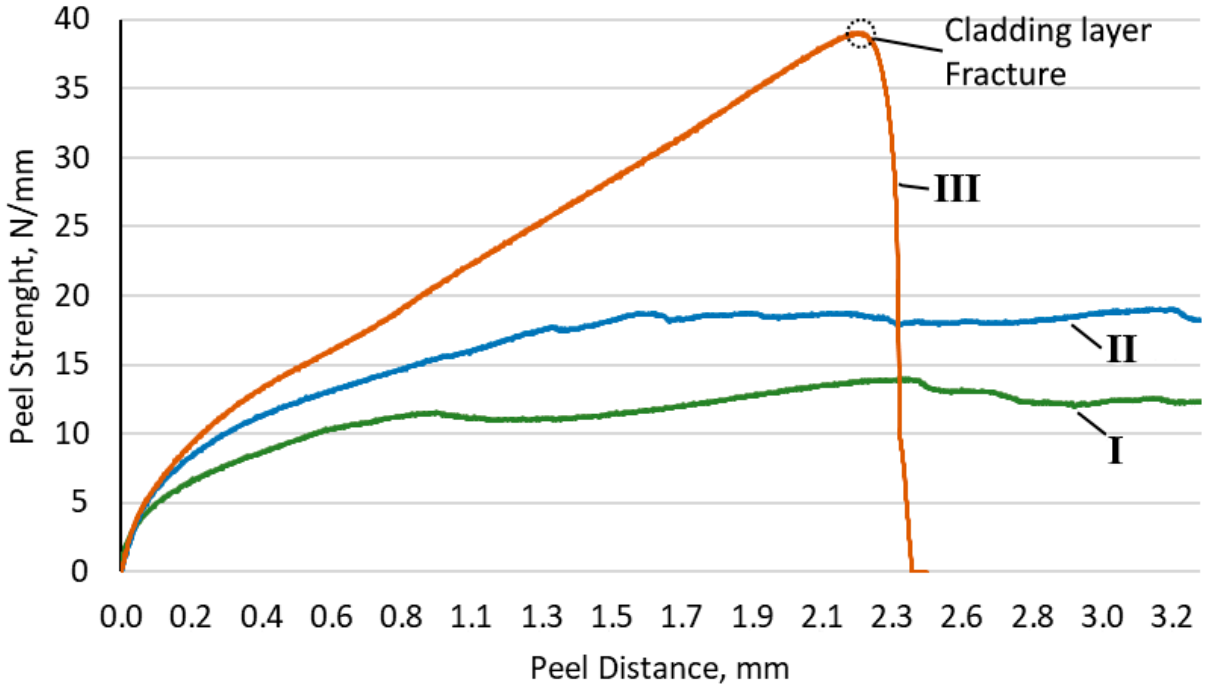

Figure 14. Peeling strength of the test samples.

4. Discussion

The simulation results do not demonstrate any significant difference between the stresses and strains for the rolling routes used. However, they indicate the presence of DC zones exhibiting the greatest change in the contact interaction between the layers during cladding. It is safe to assume that these zones originate from the specific metal flow conditions. Figure 15a shows the change in the velocity of the tracked points at the roll contact (P3), at the interlayer boundary (P1) and at ½ of the composite thickness (P4) for rolling at ε_t = 0.33. The curves are typical of longitudinal rolling and allow one to distinguish the boundary between the forward and backward slip zones at ~0.65 of the DC length. The abrupt changes in the strain (Figures 8 and 10) occur at 0.7 DC length. This can be accounted for by the significant nonuniformity of the metal flow rate distribution over the DC thickness, as can be seen from Figure 15b. One can also note that the no-slip zone is I-shaped and has an increased tool contact area, with its center (neutral section) being tilted. The latter fact originates from the difference in the parameters of the rolled metals, leading to a difference between the rolling torques at the upper and lower rolls. Thus, the metal plastic flow pattern in the deformation center that was typical of asymmetrical rolling affected the simulation results the most tangibly. Due to its influence, low strain rate zones formed, which reduced the deformation resistance of both layers. The friction stresses tend to zero in these zones.

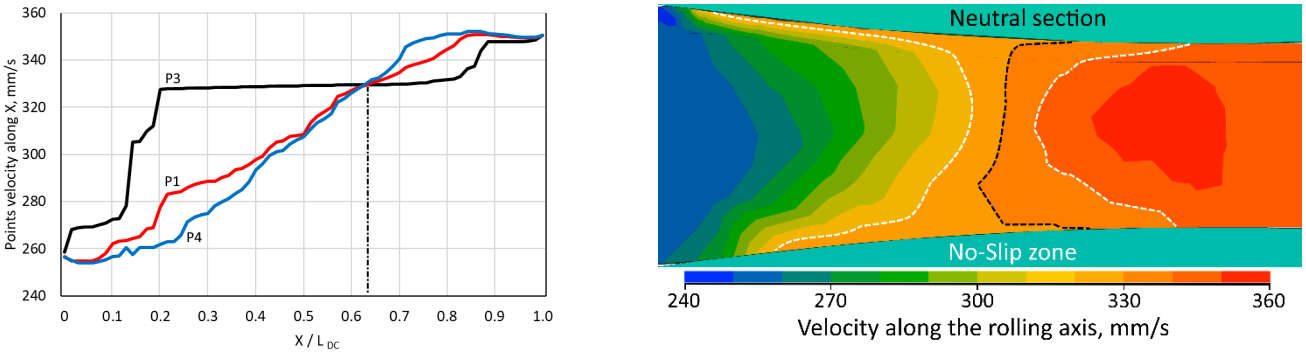

(**a**) (**b**)

Figure 15. Tracked point velocity along the X-axis (**a**) and flow rate fields in the DC (**b**).

The cladding simulation results for different deformations exhibit some ambiguity. On the one hand, greater strain strengthened the cladding layer, thus considerably reducing the ratio between the flow stresses of the base and cladding layers from 3 to 1.5 times. On the other hand, the strain magnitude affected the normal and tangential stresses between the layers, albeit slightly. One can therefore assume that the effect of the contact and interlayer friction is negligible for thin sheet rolling.

The rolling force simulation data show the best agreement with the experimental results. When increasing the true strain, the rolling force curves grow steadily by 20% (Figure 6a), with similar behavior being typical of the rolled sample peeling strength. The small discrepancy between these data can be accounted for by the effect of the DC length, which was not taken into account in this work and hence the rolling force application duration might vary. One can therefore conclude that efficient metal bonding under the experimental conditions can be guaranteed by the required rolling force and normal stress that can be achieved at elevated strain, as well as by the process duration.

By and large, comparison of the simulation data with the standpoints of the classic flat rolling theory [30,31] and recent calculation and experimental results [32–34] suggests the adequacy of the developed model and the high efficiency of the commercial software used.

5. Conclusions

- The strengthening of the softer 1050A alloy cladding layer intensified with increasing strain. The equivalent strains in the cladding/base layer contact zone were 1.0, 1.4 and 2.0 for strains of 0.26, 0.33 and 0.40, respectively. The latter fact favored the decrease in the difference between the flow stresses of the rolled layer contact surfaces.
- Study of the contact interaction between the rolled sheet layer surfaces revealed specific zones at 0.2 and 0.7 of the deformation center length along the rolling axis in which the normal stresses dominated over the tangential ones. These zones originate from the metal flow pattern in the deformation center, i.e., the absence of plastic strain in the base 2Cu2Mn alloy layer at the DC entrance and the 10 degree tilt of the neutral section due to a greater torque at the upper roll.
- The peeling strengths of the layers were 12.6 and 18.4 N/mm for roll bonding at true strains of 0.26 and 0.33, respectively. The bond strength for the 0.40 strain rolling route was higher than the 1050A alloy flow stress. The roll-bonding force simulation data show the best agreement with the experimental results. Roll bonding with a 105 kN metal pressure on the roll and a 0.40 true strain guaranteed the formation of a strong bond between the 2Cu2Mn and 1050A alloy layers.

Author Contributions: Conceptualization, A.K.; methodology, K.T.; software, S.C.; validation, K.T.; formal analysis, A.M.A.A.; investigation, A.M.A.A.; resources, A.Z.; data curation, A.Z.; writing—original draft preparation, A.K.; writing—review and editing, A.Z.; visualization, S.C.; supervision,

A.C.; project administration, A.C.; funding acquisition, A.K. All authors have read and agreed to the published version of the manuscript.

Funding: This study was carried out with the financial support of the Russian Science Foundation grant (Project No. 23-79-01172, https://rscf.ru/project/23-79-01172/ (accessed on 2024-07-25)) and the Moscow Polytechnic University within the framework of the grant named after Pyotr Kapitsa.

Data Availability Statement: The original contributions presented in the study are included in the article, further inquiries can be directed to the corresponding author.

Conflicts of Interest: The authors declare no conflicts of interest.

References

1. Kammer, C. Aluminum and aluminum alloys. In *Springer Handbook of Materials Data*; Warlimont, H., Martienssen, W., Eds.; Springer: Cham, Switzerland, 2018; pp. 161–197, ISBN 978-3-319-69743-7. https://doi.org/10.1007/978-3-319-69743-7_6.
2. Sadeghi, S.; Karimi, Z.; Fotouhi, M.; Hasani, M.; Najafabadi, M.A.; Pavlović, A. Residual stress evaluation in friction stir welding of aluminium plates by means of acoustic emission and ultrasonic waves. *FME Trans.* **2018**, *46*, 230–237. https://doi.org/10.5937/fmet1802230S.
3. Davis, J.R. *Aluminum and Aluminum Alloys*; ASM International: Materials Park, OH, USA, 2001; p. 351. Available online: https://scholar.google.com/scholar_lookup?title=Aluminum+and+Aluminum+Alloys&author=Davis,+J.R.&publication_year=2001 (accessed on 2024-07-25).
4. Sanders, R.; Staley, J.T. A History of Wrought Aluminum Alloys and Applications. *Properties and Selection of Aluminum Alloys*, Vol. 2B; ASM International: Novelty, OH, USA, 2019. https://doi.org/10.31399/asm.hb.v02b.a0006516.
5. Belov, N.A.; Akopyan, T.K.; Shurkin, P.K.; Korotkova, N.O. Comparative Analysis of Structure Evolution and Thermal Stability of Commercial AA2219 and Model Al-2 wt%Mn-2 wt%Cu Cold Rolled Alloys. *J. Alloys Compd.* **2021**, *864*, 158823. https://doi.org/10.1016/j.jallcom.2021.158823.
6. Koshmin, A.; Cherkasov, S.; Fortuna, A.; Gamin, Y.; Churyumov, A. Optimization of flat-rolling parameters for thermally stable alloy of Al-Cu-Mn System with micro additions of Si and Zr. *Metals* **2023**, *13*, 2019. https://doi.org/10.3390/met13122019.
7. Belov, N.A.; Alabin, A.N.; Matveeva, I.A. Optimization of phase composition of Al–Cu–Mn–Zr–Sc alloys for rolled products without requirement for solution treatment and quenching. *J. Alloys Compd.* **2014**, *583*, 206–213. https://doi.org/10.1016/j.jallcom.2013.08.202.
8. Belov, N.A.; Cherkasov, S.O.; Korotkova, N.O.; Yakovleva, A.O.; Tsydenov, K.A. Effect of Iron and Silicon on the Phase Composition and Microstructure of the Al–2% Cu–2% Mn (wt%) Cold Rolled Alloy. *Phys. Met. Metallogr.* **2021**, *122*, 1095–1102. https://doi.org/10.1134/S0031918X2111003X.
9. Belov, N.A.; Tsydenov, K.A.; Letyagin, N.V.; Cherkasov, S.O. Structure and mechanical properties of hot rolled sheets of Al-2% Cu-2% Mn-0.4% Si-0.2% Zr alloy subjected to friction stir welding. *Tsvetnye Met.* **2022**, *5*, 66–72. https://doi.org/10.17580/tsm.2022.05.09.
10. Akopyan, T.K.; Letyagin, N.V.; Belov, N.A.; Fortuna, A.S.; Nguen, X.D. The role of Sn trace addition in the precipitation behavior and strengthening of the wrought Al–Cu–Mn-based alloy. *J. Mater. Sci.* **2023**, *58*, 8210–8229. https://doi.org/10.1007/s10853-023-08513-4.
11. Ghali, E. *Corrosion Resistance of Aluminum and Magnesium Alloys: Understanding, Performance, and Testing*; John Wiley & Sons: Hoboken, NJ, USA, 2010. Available online: https://scholar.google.com/scholar_lookup?title=Corrosion+Resistance+of+Aluminum+and+Magnesium+Alloys:+Understanding,+Performance,+and+Testing&author=Ghali,+E.&publication_year=2010 (accessed on 2024-07-25).
12. Vargel, C. *Corrosion of Aluminium*; Elsevier: Amsterdam, The Netherlands, 2004.
13. Khan, H.A.; Asim, K.; Akram, F.; Hameed, A.; Khan, A.; Mansoor, B. Roll Bonding Processes: State-of-the-Art and Future Perspectives. *Metals* **2021**, *11*, 1344. https://doi.org/10.3390/met11091344.
14. Zixuan, L.; Shahed, R.; Tao, W.; Han, J.; Shu, X.; Pater, Z.; Huang, Q. Recent advances and trends in roll bonding process and bonding model: A review. *Chin. J. Aeronaut.* **2023**, *36*, 36–74. https://doi.org/10.1016/j.cja.2022.07.004.
15. Kobelev, A.G.; Lysak, V.I.; Chernyshev, V.N.; Kuznetsov, E.V. *Materials Science and Technology of Composite Materials*; Intermet Engineering: Moscow, Russia, 2006. (In Russian)
16. Shatalov, R.L.; Kulikov, M.A. Influence of outer parts of a strip on the deformation and force parameters of thin-sheet rolling. *Metallurgist* **2020**, *64*, 687–698. https://doi.org/10.1007/s11015-020-01045-1.
17. Zhang, W.; Bay, N. A Numerical Model for Cold Welding of Metals. *CIRP Ann.-Manuf. Technol.* **1996**, *45*, 215–220. https://doi.org/10.1016/S0007-8506(07)63050-9.
18. Bambach, M.; Pietryga, M.; Mikloweit, A.; Hirt, G. A finite element framework for the evolution of bond strength in joining-by-forming processes. *J. Mater. Process. Technol.* **2014**, *214*, 2156–2168. https://doi.org/10.1016/j.jmatprotec.2014.03.015.
19. Needleman, A. An Analysis of Decohesion along an Imperfect Interface. *Int. J. Fract.* **1990**, *42*, 21–40. https://doi.org/10.1007/BF00018611.

20. Kebriaei, R.; Vladimirov, I.N.; Reese, S. Joining of the alloys AA1050 and AA5754—Experimental characterization and multiscale modeling based on a cohesive zone element technique. *J. Mater. Process. Technol.* **2014**, *214*, 2146–2155. https://doi.org/10.1016/j.jmatprotec.2014.03.014.
21. Frolov, Y.; Nosko, M.; Samsonenko, A.; Bobukh, O.; Remez, O. Roll Bonding of Al-Based Composite Reinforced with C10 Steel Expanded Mesh Inlay. *Metals* **2021**, *11*, 1044. https://doi.org/10.3390/met11071044.
22. Frolov, Y.; Bobukh, O.; Samsonenko, A.; Nürnberger, F. Patterning of Surfaces for Subsequent Roll Bonding in a Low-Oxygen Environment Using Deformable Mesh Inlays. *J. Manuf. Mater. Process.* **2023**, *7*, 158. https://doi.org/10.3390/jmmp7050158.
23. Vlasov, A.V.; Stebunov, S.A.; Evsyukov, S.A.; Biba, N.V.; Shitikov, A.A. *Finite-Element Modeling of Technological Processes of Forging and Stamping: Textbook*; Bauman Moscow State Technical University: Moscow, Russia, 2019. (In Russian)
24. European Committee for Standardization. *Aluminium and aluminium alloys - Chemical composition and form of wrought products - Part 3: Chemical composition and form of products*; EN 573-3:2007; Brussels, Belgium, 2007.
25. Rao, K.P.; Doraivelu, S.M.; Gopinathan, V. Flow curves and deformation of materials at different temperatures and strain rates. *J. Mech. Work. Technol.* **1982**, *6*, 63–88. https://doi.org/10.1016/0378-3804(82)90020-1.
26. Aksöz, S.; Ocak, Y.; Maraşlı, N.; Çadirli, E.; Kaya, H.; Böyük, U. Dependency of the Thermal and Electrical Conductivity on the Temperature and Composition of Cu in the Al Based Al–Cu Alloys. *Exp. Therm. Fluid Sci.* **2010**, *34*, 1507–1516. https://doi.org/10.1016/j.expthermflusci.2010.07.015.
27. ASTM International. *Standard Test Method for Peel Resistance of Adhesives (T-Peel Test)*; ASTM D1876-08(2015)e1; West Conshohocken, PA, 2015. https://doi.org/10.1520/D1876-08R15E01.
28. Qin, Q.; Zhang, D.-T.; Zang, Y.; Guan, B. A simulation study on the multi-pass rolling bond of 316L/Q345R stainless clad plate. *Adv. Mech. Eng.* **2015**, *7*, 1687814015594313. https://doi.org/10.1177/1687814015594313.
29. He, Z.; Chu, Z.; Shuang, Y.; Gou, Y. The bonding mechanism and experimental verification of pilger hot rolling clad tube. *Adv. Mater. Sci. Eng.* **2020**, *2020*, 2689370. https://doi.org/10.1155/2020/2689370.
30. Kolpashnikov, A.I. *Rolling of Light Alloy Sheets*; Metallurgiya: Moscow, Russia, 1970. (In Russian)
31. Kovalev, S.I.; Koryagin, N.I.; Shirkov, I.V. *Stresses and Strains in Flat Rolling*; Metallurgiya: Moscow, Russia, 1982. (In Russian)
32. Zhang, X.; Yang, T.; Castagne, S.; Gu, C.; Wang, J. Proposal of bond criterion for hot roll bonding and its application. *Mater. Des.* **2011**, *32*, 2239–2245. https://doi.org/10.1016/j.matdes.2010.11.039.
33. Salikhyanov, D.R. Investigation of the stress-strain state at the boundary between materials during rolling of a layered composite. *Chernye Met.* **2023**, *129*, 34–39. https://doi.org/10.17580/chm.2023.09.06.
34. Salikhyanov, D.; Michurov, N. Joining of dissimilar aluminum alloys AA5154 and AA2024 by cold roll bonding. *Int. J. Adv. Manuf. Technol.* **2023**, *129*, 255–277. https://doi.org/10.1007/s00170-023-12292-2.

Disclaimer/Publisher's Note: The statements, opinions and data contained in all publications are solely those of the individual author(s) and contributor(s) and not of MDPI and/or the editor(s). MDPI and/or the editor(s) disclaim responsibility for any injury to people or property resulting from any ideas, methods, instructions or products referred to in the content.